

# RIVER AND RESERVOIR FLOW MODELLING USING THE TRANSFORMED SHALLOW WATER EQUATIONS

A. G. L. BORTHWICK

*Department of Engineering Science, University of Oxford, Oxford OX1 3PJ, U.K.*

AND

R. W. BARBER

*Department of Civil Engineering, University of Salford, Salford M5 4WT, U.K.*

## SUMMARY

This paper describes a versatile finite difference scheme for the solution of the two-dimensional shallow water equations on boundary-fitted non-orthogonal curvilinear meshes. It is believed that this is the first non-orthogonal shallow water equation model incorporating the advective acceleration terms to have been developed in the United Kingdom.

The numerical scheme has been validated against the severe condition of jet-forced flow in a circular reservoir with vertical side walls, where reflections of the initial free surface waves pose major problems in achieving a stable solution. Furthermore, the validation exercises are designed to test the computer model for artificial diffusion, which may be a consequence of the numerical scheme adopted to stabilize the shallow water equations. The model is shown to be capable of simulating the flow conditions in an irregularly shaped domain typical of the geometries frequently encountered in civil engineering river basin management.

KEY WORDS Shallow water equations Boundary-fitted co-ordinate systems Non-orthogonal curvilinear meshes

## 1. INTRODUCTION

In the past two decades the numerical modelling of rivers, estuaries, harbours and reservoirs has usually been undertaken using Cartesian grid finite difference discretizations of the shallow water equations. In the U.K. most models are based on the work of Falconer,<sup>1,2</sup> who derived his approach from that of Leendertse.<sup>3</sup> Unfortunately, Cartesian grid schemes have the disadvantage that it is difficult to model curved perimeters accurately. Leendertse,<sup>3</sup> Abbott *et al.*<sup>4</sup> and Hodgins<sup>5</sup> approximated the curvature of the boundary by using a staircase of points to follow the perimeter. An alternative method, utilized by Kuipers and Vreugdenhil<sup>6</sup> and Falconer,<sup>1,2</sup> also employs a stepped pattern to follow the curved boundary, but unlike the Leendertse approach where the staircase straddles the flow domain, the hydraulic region is located entirely *within* the numerical grid. Interpolation has to be used to redistribute the fluid in the boundary regions so that overall fluid mass is conserved. In either case, unnecessary (or spurious) vorticity may be generated at each of the boundary nodes. Moreover, in Cartesian schemes it is relatively difficult to concentrate extra grid refinement in zones of interest. At first sight it may appear that finite element methods are ideally suited for this type of application. However, as discussed by Weare,<sup>7</sup> the large bandwidth of the global stiffness matrix employed in the finite element methodology

means that the technique is computationally less efficient than corresponding finite difference schemes.

Boundary-fitted co-ordinate systems provide an approach which combines the best aspects of finite difference discretization with the grid flexibility usually attributed to finite element procedures. In essence, a coupled pair of elliptic equations is solved to generate the grid, the governing flow equations are rewritten in curvilinear form and then discretized using finite differences ready for solution by computer. The idea behind boundary-fitted systems originated in the U.S. aerospace industry in the early 1970s as a response to NASA's requirement to predict high-velocity flow patterns around irregularly shaped space vehicles. Since then, boundary-fitted systems have been utilized for the solution of a wide variety of fluid dynamic problems in aeronautical and mechanical engineering. Surprisingly, even though numerical grid generation techniques have been thoroughly documented, few publications are as yet available concerning the solution of the two-dimensional shallow water equations using curvilinear co-ordinates. The earliest studies on the complete transformed non-linear shallow water equations were conducted by Johnson and co-workers<sup>8-10</sup> in the United States. Other curvilinear models include Häuser *et al.*'s and Raghunath *et al.*'s numerical scheme for the linearized shallow water equations.<sup>11-13</sup> Wjibenga<sup>14,15</sup> and Willemse *et al.*<sup>16</sup> of Delft Hydraulics in The Netherlands have developed an alternative computational approach requiring an orthogonal curvilinear mesh.

At the onset of any numerical investigation using boundary-fitted techniques it is necessary to decide whether the co-ordinate system should be orthogonal or non-orthogonal. The former method is attractive since Cartesian solution procedures for the governing hydrodynamic equations can be modified with little additional effort. However, the orthogonality constraint during mesh generation severely limits the distribution of co-ordinate lines around complex topographical features such as headlands and bays. On the other hand, non-orthogonal grid systems allow more flexibility in the internal grid point distribution but have the drawback that the governing equations of motion are considerably more complex than their orthogonal counterparts. In the present study the ability to stretch and distort the internal grid nodes without placing any restriction on the disposition of the boundary grid points was judged to be sufficient incentive to tolerate the disadvantages of using a non-orthogonal mesh.

It is the purpose of this paper to describe a primitive variable shallow water equation solver for arbitrary non-orthogonal meshes. The model has been designed specifically for flow prediction in shallow watercourses of irregular shape. It consists essentially of two modules: the first generates the non-orthogonal grid within the prescribed flow domain, the second solves the transformed non-linear shallow water equations in a stable and non-diffusive manner.

## 2. METHODOLOGY OF GRID GENERATION

The initial step consists of producing a boundary-fitted grid of the physical flow domain; this is achieved using the elliptic grid generation technique proposed by Thompson *et al.*<sup>17,18</sup> A pair of Poisson equations is used to define the mapping from the physical domain to the transformed (or 'computational') plane:

$$\xi_{xx} + \xi_{yy} = P(\xi, \eta), \quad (1a)$$

$$\eta_{xx} + \eta_{yy} = Q(\xi, \eta). \quad (1b)$$

The weighting functions  $P$  and  $Q$  (described in detail by Thompson *et al.*<sup>18</sup>) cause the physical co-ordinate lines to concentrate as desired; they are often useful to counteract grid skewness and excessive cell size variation in regions of large boundary curvature. Since all numerical com-

putations are to be performed in the transformed plane, the system of Poisson equations in (1) must be rewritten in terms of the computational co-ordinates  $(\xi, \eta)$ . It can be shown that the dependent and independent variables can be interchanged to give

$$\alpha x_{\xi\xi} - 2\beta x_{\xi\eta} + \gamma x_{\eta\eta} + J^2(Px_{\xi} + Qx_{\eta}) = 0, \tag{2a}$$

$$\alpha y_{\xi\xi} - 2\beta y_{\xi\eta} + \gamma y_{\eta\eta} + J^2(Py_{\xi} + Qy_{\eta}) = 0, \tag{2b}$$

where

$$\alpha = x_{\eta}^2 + y_{\eta}^2, \quad \beta = x_{\xi}x_{\eta} + y_{\xi}y_{\eta}, \quad \gamma = x_{\xi}^2 + y_{\xi}^2,$$

and  $J = x_{\xi}y_{\eta} - x_{\eta}y_{\xi}$  is the Jacobian of the transformation.

The quasi-linear elliptic equations given in (2) relate the physical co-ordinates  $(x, y)$  of the mesh points to the transformed co-ordinates  $(\xi, \eta)$ . Although the transformed expressions are more complex than equations (1a) and (1b), boundary conditions can now be specified along the straight edges of the computational domain. This permits the accurate use of finite difference techniques for numerically solving the grid generation equations. The mapping expressions shown in (2) are rewritten as finite differences and then solved iteratively using a successive over-relaxation procedure. Furthermore, all subsequent hydrodynamic computations are also performed in terms of the  $(\xi, \eta)$  co-ordinate system.

### 3. CARTESIAN GOVERNING HYDRODYNAMIC EQUATIONS

Assuming the location of the bed is constant with time (i.e. there is no sediment deposition or erosion), the depth-averaged continuity equation for a Cartesian reference frame is given by

$$\frac{\partial \zeta}{\partial t} + \frac{\partial(UD)}{\partial x} + \frac{\partial(VD)}{\partial y} = 0, \tag{3}$$

where  $x$  and  $y$  are the horizontal co-ordinates,  $t$  is the time,  $\zeta$  is the surface elevation above an arbitrary datum,  $D = h + \zeta$  is the local water depth, where  $h$  is the distance between the bed and the datum, and  $U$  and  $V$  are depth-averaged velocity components.

The non-conservative depth-integrated momentum equations in the  $x$ - and  $y$ -direction respectively are given by

$$\frac{\partial U}{\partial t} + U \frac{\partial U}{\partial x} + V \frac{\partial U}{\partial y} = f_c V - g \frac{\partial \zeta}{\partial x} + \frac{\tau_{wx} - \tau_{bx}}{\rho D} + \frac{1}{\rho D} \left( \frac{\partial(DT_{xx})}{\partial x} + \frac{\partial(DT_{xy})}{\partial y} \right), \tag{4a}$$

$$\frac{\partial V}{\partial t} + U \frac{\partial V}{\partial x} + V \frac{\partial V}{\partial y} = -f_c U - g \frac{\partial \zeta}{\partial y} + \frac{\tau_{wy} - \tau_{by}}{\rho D} + \frac{1}{\rho D} \left( \frac{\partial(DT_{xy})}{\partial x} + \frac{\partial(DT_{yy})}{\partial y} \right), \tag{4b}$$

where  $\rho$  is the fluid density,  $g$  is the acceleration due to gravity,  $f_c$  is the Coriolis parameter,  $\tau_w$  and  $\tau_b$  are wind and bed friction stresses and  $T_{xx}$ ,  $T_{xy}$  and  $T_{yy}$  are effective stress components (as defined by Kuipers and Vreugdenhil<sup>6</sup>).

Implementation of the Boussinesq eddy viscosity concept allows the effective stresses to be written as

$$T_{xx} = 2\rho\tilde{\nu}_t \frac{\partial U}{\partial x}, \quad T_{xy} = \rho\tilde{\nu}_t \left( \frac{\partial U}{\partial y} + \frac{\partial V}{\partial x} \right), \quad T_{yy} = 2\rho\tilde{\nu}_t \frac{\partial V}{\partial y}, \tag{5}$$

where  $\tilde{\nu}_t$  is the eddy viscosity coefficient and the overtilde indicates that the variable is not a true depth-averaged quantity but is a value which produces the appropriate depth-integrated stress

when inserted into equation (5). In the present study two methods have been used to evaluate the eddy viscosity coefficient, namely constant and depth-averaged eddy viscosity models.

A constant eddy viscosity approach is utilized for validation purposes because it enables direct comparisons with data from alternative Navier–Stokes simulations at low Reynolds numbers. Alternatively, a simple algebraic depth-averaged eddy viscosity relationship can be employed to determine the spatial distribution of  $\tilde{\nu}_t$ , namely

$$\tilde{\nu}_t = \frac{5.9D\sqrt{g(U^2 + V^2)^{1/2}}}{C}, \quad (6)$$

where  $C$  is the Chezy coefficient. The definition of  $\tilde{\nu}_t$  in equation (6) is based on the proposition by Kuipers and Vreugdenhil<sup>6</sup> that the eddy viscosity is of the same order of magnitude as the longitudinal diffusivity of dye in an open channel. The above expression was also utilised by Falconer,<sup>1</sup> who allowed the eddy viscosity to vary across the flow field in accordance with the local velocity vectors. As Kuipers and Vreugdenhil point out,<sup>6</sup> the most questionable assumption about the formula arises from the fact that momentum can be transferred by surface elevation gradients, whereas there is no comparable mechanism for the transport of matter in the dispersion equation.

The components of bed shear stress ( $\tau_{bx}$  and  $\tau_{by}$ ) are related to the depth-averaged velocity components via a quadratic friction law,

$$\frac{\tau_{bx}}{\rho} = c_f U(U^2 + V^2)^{1/2}, \quad \frac{\tau_{by}}{\rho} = c_f V(U^2 + V^2)^{1/2}, \quad (7)$$

where  $c_f$  is an empirical friction coefficient which depends upon the bottom roughness. For smooth beds the friction coefficient is determined solely by the Reynolds number and can be approximated from the formula presented by Schlichting<sup>19</sup> for open channel flow,

$$c_f = 0.027 \left( \frac{\nu}{UR} \right)^{1/4}, \quad (8)$$

where  $\nu$  is the coefficient of kinematic viscosity and  $R$  is the hydraulic radius of the channel cross-section. With rough beds  $c_f$  can be determined either from the Chezy friction law,

$$c_f = \frac{g}{C^2}, \quad (9)$$

or alternatively from Manning's equation,

$$c_f = \frac{n^2 g}{D^{1/3}}, \quad (10)$$

where  $C$  is the Chezy coefficient and  $n$  is the Manning roughness factor.

#### 4. TRANSFORMED GOVERNING EQUATIONS

Since the numerical computations are performed on a non-orthogonal mesh, it is necessary to convert the previously presented Cartesian formulae into transformed equations written in terms of the boundary-fitted co-ordinates  $\xi$  and  $\eta$ . Following the work of Johnson,<sup>8,9</sup> Johnson *et al.*,<sup>10</sup> Häuser *et al.*,<sup>11,12</sup> and Raghunath *et al.*,<sup>13</sup> only the independent variables ( $x, y$ ) are transformed. This overcomes the difficulties associated with the unwieldy diffusive terms which are encoun-

tered when implementing contravariant/covariant velocity techniques on non-orthogonal coordinate systems.<sup>20</sup>

The transformation of the Cartesian shallow water equations is accomplished using the non-conservative derivative relationships presented by Thompson *et al.*,<sup>17</sup>

$$f_x = \frac{\partial f}{\partial x} = \frac{\partial(f, y)}{\partial(\xi, \eta)} \div \frac{\partial(x, y)}{\partial(\xi, \eta)} = \frac{1}{J}(y_\eta f_\xi - f_\eta y_\xi), \quad (11a)$$

$$f_y = \frac{\partial f}{\partial y} = \frac{\partial(x, f)}{\partial(\xi, \eta)} \div \frac{\partial(x, y)}{\partial(\xi, \eta)} = \frac{1}{J}(x_\xi f_\eta - f_\xi x_\eta), \quad (11b)$$

where  $f$  denotes a differentiable function of  $x$  and  $y$ .

Substituting the above expressions into all partial derivatives involving  $x$  or  $y$  in the governing Cartesian equations of motion leads to the depth-averaged continuity equation being recast as

$$\frac{\partial \zeta}{\partial t} + \frac{1}{J} \left( y_\eta \frac{\partial(UD)}{\partial \xi} - y_\xi \frac{\partial(UD)}{\partial \eta} + x_\xi \frac{\partial(VD)}{\partial \eta} - x_\eta \frac{\partial(VD)}{\partial \xi} \right) = 0, \quad (12)$$

whilst the non-conservative momentum relationships are rewritten as

$$\begin{aligned} \frac{\partial U}{\partial t} + \frac{1}{J} \left( y_\eta U \frac{\partial U}{\partial \xi} - y_\xi U \frac{\partial U}{\partial \eta} + x_\xi V \frac{\partial U}{\partial \eta} - x_\eta V \frac{\partial U}{\partial \xi} \right) - f_c V + \frac{g}{J} \left( y_\eta \frac{\partial \zeta}{\partial \xi} - y_\xi \frac{\partial \zeta}{\partial \eta} \right) \\ - \frac{\tau_{wx} - \tau_{bx}}{\rho D} - \frac{1}{\rho DJ} \left( y_\eta \frac{\partial(DT_{xx})}{\partial \xi} - y_\xi \frac{\partial(DT_{xx})}{\partial \eta} + x_\xi \frac{\partial(DT_{xy})}{\partial \eta} - x_\eta \frac{\partial(DT_{xy})}{\partial \xi} \right) = 0, \end{aligned} \quad (13a)$$

$$\begin{aligned} \frac{\partial V}{\partial t} + \frac{1}{J} \left( y_\eta U \frac{\partial V}{\partial \xi} - y_\xi U \frac{\partial V}{\partial \eta} + x_\xi V \frac{\partial V}{\partial \eta} - x_\eta V \frac{\partial V}{\partial \xi} \right) + f_c U + \frac{g}{J} \left( x_\xi \frac{\partial \zeta}{\partial \eta} - x_\eta \frac{\partial \zeta}{\partial \xi} \right) \\ - \frac{\tau_{wy} - \tau_{by}}{\rho D} - \frac{1}{\rho DJ} \left( y_\eta \frac{\partial(DT_{xy})}{\partial \xi} - y_\xi \frac{\partial(DT_{xy})}{\partial \eta} + x_\xi \frac{\partial(DT_{yy})}{\partial \eta} - x_\eta \frac{\partial(DT_{yy})}{\partial \xi} \right) = 0. \end{aligned} \quad (13b)$$

The effective stress equations are also transformed into the  $(\xi, \eta)$  co-ordinate system:

$$\begin{aligned} T_{xx} &= 2\rho\tilde{\nu}_t \frac{1}{J}(y_\eta U_\xi - y_\xi U_\eta), \\ T_{xy} &= \rho\tilde{\nu}_t \frac{1}{J}(x_\xi U_\eta - x_\eta U_\xi + y_\eta V_\xi - y_\xi V_\eta), \\ T_{yy} &= 2\rho\tilde{\nu}_t \frac{1}{J}(x_\xi V_\eta - x_\eta V_\xi). \end{aligned} \quad (14)$$

## 5. NUMERICAL SCHEME

The transformed governing equations (12)–(14) were discretized on a staggered  $(\xi, \eta)$  grid and solved using a semi-implicit alternating direction finite difference scheme. In contrast to the earlier work of Johnson and co-workers<sup>8–10</sup> and Häuser *et al.*<sup>11,12</sup> where the  $U$ - and  $V$ -velocity components were placed at the same location, the present velocity variables were fully staggered as illustrated in Figure 1. Although this arrangement requires additional spatial averaging, the advantage of the present layout is that the scheme reverts to a standard Cartesian discretization whenever a uniform orthogonal grid aligned with the co-ordinate axes is employed.

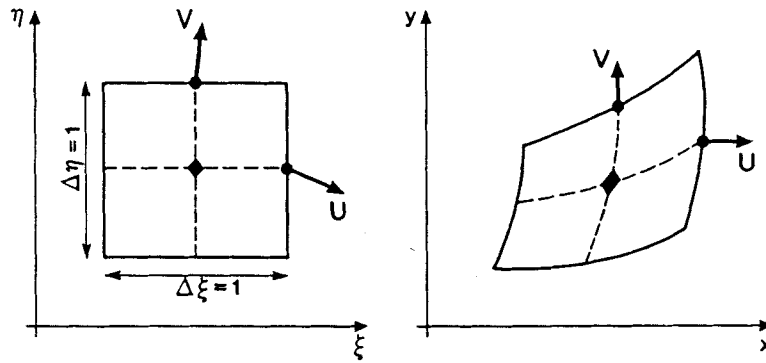


Figure 1. Cell definition

In order that the geometric derivatives ( $x_\xi$ ,  $x_\eta$ ,  $y_\xi$  and  $y_\eta$ ) could be specified at the cell centres and the cell mid-faces, the co-ordinate mesh for the required flow domain was generated with twice as many cells in each direction than the number required for the eventual hydrodynamic mesh. Two interrelated spatial indexing systems were formulated:  $i$  and  $j$  refer to the variables  $U$ ,  $V$ ,  $\zeta$ ,  $h$  and  $D$ , whilst  $I$  and  $J$  define the location of the geometric variables. This split system ensures that the arrays used to store the hydrodynamic variables are of the minimum possible size. Simple arithmetic expressions can be used to 'translate' between indexing systems. For example, referring to Figure 2, if the  $x$ -momentum equation is to be updated at position  $U_{i,j}$ , then the transformation derivatives applicable to this particular point are stored at the fine grid location  $I = 2i$ ,  $J = 2j - 1$ .

$\Delta\xi$  and  $\Delta\eta$  are defined as the distances in the transformed domain between the velocity vector positions. Since the range of the co-ordinates  $\xi$  and  $\eta$  in the computational plane is completely arbitrary, the mesh increments  $\Delta\xi$  and  $\Delta\eta$  are specified, for convenience, as unity. Consequently, the geometric variables are defined on a finite difference mesh with cell increments of 0.5.

A further index,  $n$ , is now introduced to denote the time level of the discretized hydrodynamic variables. The alternating direction algorithm splits each time step into two intervals. In the first half-time step, derivatives with respect to  $\xi$  are advanced from  $t = n\Delta t$  to  $t = (n + \frac{1}{2})\Delta t$  whilst derivatives involving  $\eta$  are held at  $t = n\Delta t$ . In the second directional 'release',  $\xi$ -derivatives are held at  $t = (n + \frac{1}{2})\Delta t$  whilst  $\eta$ -derivatives are advanced from  $t = (n + \frac{1}{2})\Delta t$  to  $t = (n + 1)\Delta t$ . Non-derivative expressions (e.g. bottom friction and the Coriolis term) are evaluated at  $t = (n + \frac{1}{2})\Delta t$  for both stages of the cycle. The procedure can be demonstrated with respect to the transformed  $x$ -momentum equation (13a).

*Step 1:  $\xi$ -direction release*

$$\begin{aligned} & \frac{U^{n+1/2} - U^n}{\frac{1}{2}\Delta t} + \frac{1}{J} \left( y_\eta U^{n+1/2} \frac{\delta U^{n+1/2}}{\delta \xi} - y_\xi U^n \frac{\delta U^n}{\delta \eta} + x_\xi V^n \frac{\delta U^n}{\delta \eta} - x_\eta V^{n+1/2} \frac{\delta U^{n+1/2}}{\delta \xi} \right) \\ & - f_c V^{n+1/2} + \frac{g}{J} \left( y_\eta \frac{\delta \zeta^{n+1/2}}{\delta \xi} - y_\xi \frac{\delta \zeta^n}{\delta \eta} \right) - \frac{\tau_{wx}^{n+1/2} - \tau_{bx}^{n+1/2}}{\rho D^{n+1/2}} \\ & - \frac{1}{\rho J} \left[ \frac{1}{D^{n+1/2}} \left( y_\eta \frac{\delta(DT_{xx})^{n+1/2}}{\delta \xi} - x_\eta \frac{\delta(DT_{xy})^{n+1/2}}{\delta \xi} \right) - \frac{1}{D^n} \left( y_\xi \frac{\delta(DT_{xx})^n}{\delta \eta} - x_\xi \frac{\delta(DT_{xy})^n}{\delta \eta} \right) \right] = 0. \quad (15a) \end{aligned}$$

Step 2:  $\eta$ -direction release

$$\begin{aligned} & \frac{U^{n+1} - U^{n+1/2}}{\frac{1}{2}\Delta t} + \frac{1}{J} \left( y_\eta U^{n+1/2} \frac{\delta U^{n+1/2}}{\delta \xi} - y_\xi U^{n+1} \frac{\delta U^{n+1}}{\delta \eta} + x_\xi V^{n+1} \frac{\delta U^{n+1}}{\delta \eta} - x_\eta V^{n+1/2} \frac{\delta U^{n+1/2}}{\delta \xi} \right) \\ & - f_c V^{n+1/2} + \frac{g}{J} \left( y_\eta \frac{\delta \zeta^{n+1/2}}{\delta \xi} - y_\xi \frac{\delta \zeta^{n+1}}{\delta \eta} \right) - \frac{\tau_{wx}^{n+1/2} - \tau_{bx}^{n+1/2}}{\rho D^{n+1/2}} \\ & - \frac{1}{\rho J} \left[ \frac{1}{D^{n+1/2}} \left( y_\eta \frac{\delta(DT_{xx})^{n+1/2}}{\delta \xi} - x_\eta \frac{\delta(DT_{xy})^{n+1/2}}{\delta \xi} \right) \right. \\ & \left. - \frac{1}{D^{n+1}} \left( y_\xi \frac{\delta(DT_{xx})^{n+1}}{\delta \eta} - x_\xi \frac{\delta(DT_{xy})^{n+1}}{\delta \eta} \right) \right] = 0. \end{aligned} \tag{15b}$$

The symbol  $\delta$  represents a second-order finite-difference approximation.

By adding the above equations for the two half-time steps, it can be shown that the combined effect of Steps 1 and 2 results in an equation which is fully centred in time, provided that each term is evaluated at the correct time level. As a consequence, the ADI scheme has a formal temporal accuracy of  $\Delta t^2$ . However, because the non-orthogonal hydrodynamic equations contain approximately twice as many terms as their Cartesian counterparts, it is not possible to achieve second-order accuracy in time using a single ADI cycle because certain terms have to be lagged in order to achieve a closed solution. Thus second-order temporal accuracy can only be achieved via an iterative technique which obtains improved estimates for the otherwise lagged variables.

### 5.1. Control of non-linear instability

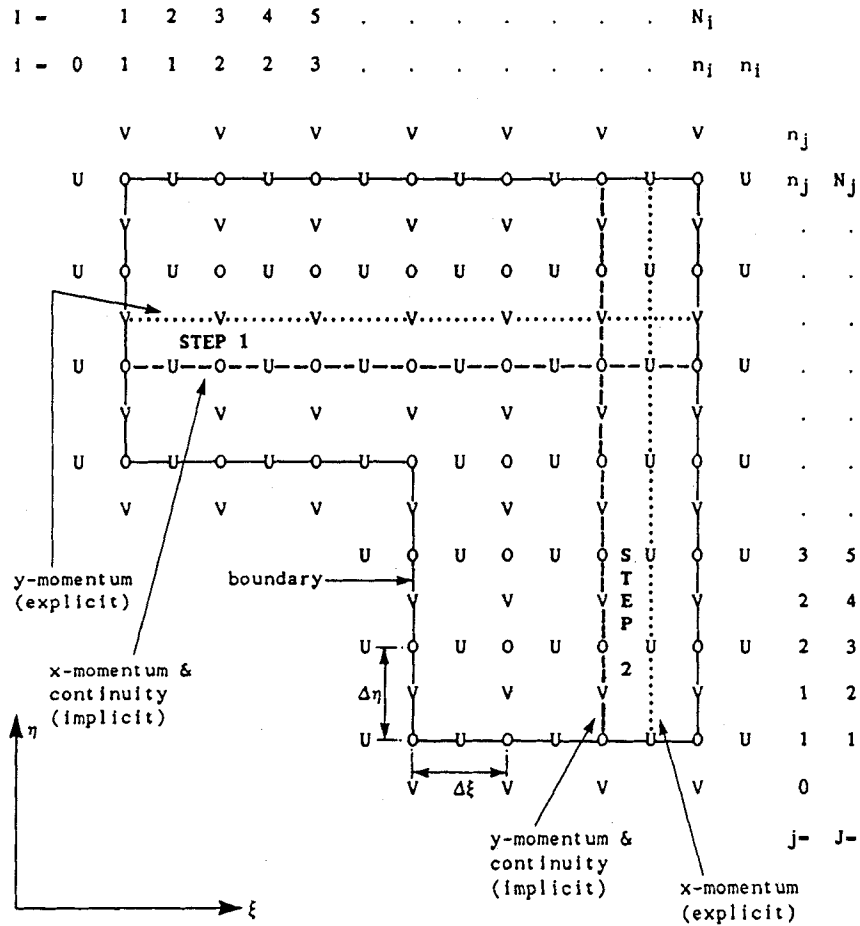
The inclusion of the non-linear advective acceleration terms in the  $x$ - and  $y$ -momentum equations will often produce destabilizing effects in the numerical scheme. These instabilities are most troublesome when modelling hydraulic regimes with strong recirculating regions and low values of eddy viscosity coefficient. Non-linear instabilities lead to severe grid scale oscillations of the velocity field (which eventually overwhelm the true numerical solution) and are caused by the discretization process preventing the transfer of turbulence energy to eddies smaller than the resolution of the computational mesh. Central difference approximations of the non-linear accelerations are the most unstable form of differencing and can only be used in conjunction with large values of eddy viscosity coefficient. Therefore the present numerical simulation employs a second-order upwind differencing technique based upon proposals by Stelling,<sup>21</sup> Stelling and Willemse<sup>22</sup> and Willemse *et al.*<sup>16</sup> The treatment of the advective acceleration terms eliminates grid scale numerical instabilities whilst minimizing artificial viscosity. It should be noted that the non-orthogonal transformation procedure of the present numerical scheme precludes the use of Stelling's original shallow water equation technique, which is only valid for orthogonal co-ordinate systems.

All spatial derivatives in the transformed momentum equations are approximated by central differences except for the *cross-advective* terms. For the  $x$ -momentum equation (13a) these are

$$y_\xi U \frac{\partial U}{\partial \eta}, \quad x_\xi V \frac{\partial U}{\partial \eta}, \tag{16a}$$

whilst for the  $y$ -momentum equation (13b) the cross-advective accelerations are

$$y_\eta U \frac{\partial V}{\partial \xi}, \quad x_\eta V \frac{\partial V}{\partial \xi}. \tag{16b}$$



KEY

- : boundary.
- - - : represents an implicit line-wise flow calculation.
- ..... : symbolizes explicit computations.
- STEP 1 :  $\xi$ -direction release :  $t = n\Delta t \rightarrow (n + \frac{1}{2})\Delta t$ .
- STEP 2 :  $\eta$ -direction release :  $t = (n + \frac{1}{2})\Delta t \rightarrow (n + 1)\Delta t$ .

Figure 2. Diagrammatic representation of semi-implicit numerical scheme: transformed  $(\xi, \eta)$  plane



The terms shown above are evaluated either as weighted central differences or as second-order (i.e. quadratic) upwind differences, depending upon the particular stage of the computational scheme. For example, in the  $\xi$ -direction release the cross-advective terms in the  $x$ -momentum equation are both calculated using weighted central differences, i.e.

$$y_{\xi} U \frac{\partial U}{\partial \eta} = y_{\xi} U \left( \frac{1}{3} D_{2\eta} U + \frac{2}{3} D_{1\eta} U \right) \quad (17a)$$

where  $D_{1\eta} U$  is the 'standard' central difference approximation to  $\partial U / \partial \eta$  (evaluated over two grid increments) and  $D_{2\eta} U$  is the central difference approximation to  $\partial U / \partial \eta$  (evaluated over four grid increments). Thus

$$\begin{aligned} y_{\xi} U \frac{\partial U}{\partial \eta} &= y_{\xi} U_{i,j}^n \left( \frac{1}{3} \frac{U_{i,j+2}^n - U_{i,j-2}^n}{4} + \frac{2}{3} \frac{U_{i,j+1}^n - U_{i,j-1}^n}{2} \right) \\ &= y_{\xi} U_{i,j}^n \frac{U_{i,j+2}^n - U_{i,j-2}^n + 4(U_{i,j+1}^n - U_{i,j-1}^n)}{12} \end{aligned} \quad (17b)$$

and similarly

$$x_{\xi} V \frac{\partial U}{\partial \eta} = x_{\xi} \bar{V}^n \frac{U_{i,j+2}^n - U_{i,j-2}^n + 4(U_{i,j+1}^n - U_{i,j-1}^n)}{12}, \quad (18)$$

where the overbar indicates that the hydrodynamic variable is obtained by four-point averaging.

During the  $\eta$ -direction release (Step 2) the  $x$ -momentum cross-advective terms are differenced using a combination of weighted central and quadratic upwind expressions. Since the boundary-fitted co-ordinate meshes are generated with the  $y$ - and  $\eta$ -co-ordinate axes in the same approximate direction, the cross-advective term  $x_{\xi} V \partial U / \partial \eta$  can use the sign of the  $V$ -velocity component to determine the direction of the upwind finite difference expression for  $\partial U / \partial \eta$ . On the other hand, the derivative  $y_{\xi} U \partial U / \partial \eta$  is calculated using a weighted central difference formula because the  $U$ -velocity direction is approximately normal to the  $\eta$ -direction. Consequently, the cross-advective derivatives during the  $\eta$ -direction release are discretized as

$$x_{\xi} V \frac{\partial U}{\partial \eta} = \begin{cases} x_{\xi} \bar{V}^{n+1} \left( \frac{3}{2} U_{i,j}^{n+1} - 2U_{i,j-1}^{n+1} + \frac{1}{2} U_{i,j-2}^{n+1} \right), & \text{if } \bar{V}^{n+1} > 0, \\ x_{\xi} \bar{V}^{n+1} \left( -\frac{3}{2} U_{i,j}^{n+1} + 2U_{i,j+1}^{n+1} - \frac{1}{2} U_{i,j+2}^{n+1} \right), & \text{if } \bar{V}^{n+1} < 0, \end{cases} \quad (19a)$$

and

$$y_{\xi} U \frac{\partial U}{\partial \eta} = y_{\xi} U_{i,j}^{n+1} \frac{U_{i,j+2}^{n+1} - U_{i,j-2}^{n+1} + 4(U_{i,j+1}^{n+1} - U_{i,j-1}^{n+1})}{12}. \quad (19b)$$

The same principle is employed for the  $y$ -momentum cross-advective components: Step 1 uses upwind differencing for the term  $y_{\eta} U \partial V / \partial \xi$  and weighted central differences for  $x_{\eta} V \partial V / \partial \xi$  whilst Step 2 employs weighted central differences for both these terms.

## 5.2. Numerical discretization

For brevity, only the  $\xi$ -direction ADI discretization of the  $x$ -momentum equation will be presented. A more detailed discussion of the computational scheme can be found in Reference 23. During the  $\xi$ -direction release all derivatives with respect to  $\xi$  are written at the advanced time level  $t = (n + \frac{1}{2})\Delta t$  whereas derivatives involving  $\eta$  are held at  $t = n\Delta t$ . All non-derivative expressions (e.g. bottom friction and the Coriolis term) are also evaluated at the advanced time stage. Thus the transformed  $x$ -momentum equation for the first half-time step may be discretized and

rearranged to give

$$-a_{i,j}\zeta_{i,j}^{n+1/2} + b_{i,j}U_{i,j}^{n+1/2} - c_{i,j}\zeta_{i+1,j}^{n+1/2} = k_{i,j}, \tag{20}$$

where

$$a_{i,j} = \frac{g\Delta t}{2} \frac{y_{\eta_{i,j}}}{\text{JAC}_{I,J}}, \quad b_{i,j} = 1.0 + \frac{\Delta t}{2} \frac{y_{\eta_{i,j}}}{\text{JAC}_{I,J}} \text{UD}1^{n+1/2}, \quad c_{i,j} = -\frac{g\Delta t}{2} \frac{y_{\eta_{i,j}}}{\text{JAC}_{I,J}} = -a_{i,j},$$

$$k_{i,j} = U_{i,j}^n + \frac{\Delta t}{2} \left( \frac{1}{\text{JAC}_{I,J}} (y_{\xi_{i,j}} U_{i,j}^n \text{UD}2^n - x_{\xi_{i,j}} \bar{V}^n \text{UD}2^n \right.$$

$$\left. + x_{\eta_{i,j}} \bar{V}^{n+1/2} \text{UD}1^{n+1/2} + g y_{\xi_{i,j}} \text{ZETAD}^n \right) + f_c \bar{V}^{n+1/2} - F_{bx} + F_{wx} + T_x.$$

Here JAC denotes the Jacobian in order to avoid confusion with the spatial index  $J$  and

$$\text{UD}1^{n+1/2} = \frac{U_{i+1,j}^{n+1/2} - U_{i-1,j}^{n+1/2}}{2},$$

$$\text{UD}2^n = \frac{U_{i,j+2}^n - U_{i,j-2}^n + 4(U_{i,j+1}^n - U_{i,j-1}^n)}{12}$$

(weighted central difference approximation to  $\partial U/\partial \eta$ ),

$$\bar{V}^{n+1/2} = \frac{V_{i,j}^{n+1/2} + V_{i+1,j}^{n+1/2} + V_{i+1,j-1}^{n+1/2} + V_{i,j-1}^{n+1/2}}{4},$$

$$\bar{V}^n = \frac{V_{i,j}^n + V_{i+1,j}^n + V_{i+1,j-1}^n + V_{i,j-1}^n}{4},$$

$$\text{ZETAD}^n = \frac{\zeta_{i,j+1}^n + \zeta_{i+1,j+1}^n - \zeta_{i,j-1}^n - \zeta_{i+1,j-1}^n}{4},$$

$$\text{D1} = \frac{D_{i,j}^{n+1/2} + D_{i+1,j}^{n+1/2}}{2},$$

$$\text{D2} = \frac{D_{i,j}^n + D_{i+1,j}^n}{2},$$

$$\text{SD1} = D_{i,j+1}^n + D_{i+1,j+1}^n,$$

$$\text{SD2} = D_{i,j-1}^n + D_{i+1,j-1}^n,$$

$$F_{bx} = \frac{\tau_{bx}^{n+1/2}}{\rho \text{D1}},$$

$$F_{wx} = \frac{\tau_{wx}^{n+1/2}}{\rho \text{D1}},$$

$$\text{T1} = y_{\eta_{i,j}} (D_{i+1,j}^{n+1/2} T_{xx_{i+1,j}}^{n+1/2} - D_{i,j}^{n+1/2} T_{xx_{i,j}}^{n+1/2}),$$

$$\text{T2} = -y_{\xi_{i,j}} \frac{1}{8} [\text{SD1}(T_{xx_{i,j+1}}^n + T_{xx_{i+1,j+1}}^n) - \text{SD2}(T_{xx_{i,j-1}}^n + T_{xx_{i+1,j-1}}^n)],$$

$$\text{T3} = x_{\xi_{i,j}} \frac{1}{8} [\text{SD1}(T_{xy_{i,j+1}}^n + T_{xy_{i+1,j+1}}^n) - \text{SD2}(T_{xy_{i,j-1}}^n + T_{xy_{i+1,j-1}}^n)],$$

$$\text{T4} = -x_{\eta_{i,j}} (D_{i+1,j}^{n+1/2} T_{xy_{i+1,j}}^{n+1/2} - D_{i,j}^{n+1/2} T_{xy_{i,j}}^{n+1/2}),$$

$$T_x = \frac{1}{\rho \text{JAC}_{I,J}} \left( \frac{\text{T1} + \text{T4}}{\text{D1}} + \frac{\text{T2} + \text{T3}}{\text{D2}} \right).$$

The right-hand side of equation (20) contains advanced  $U$ - and  $V$ -velocity components in the terms  $\text{UD}1^{n+1/2}$ ,  $\bar{V}^{n+1/2}$  and  $F_{bx}$ , together with advanced effective stress components in  $T_x$ . Furthermore, the coefficient  $b_{i,j}$  involves  $\text{UD}1^{n+1/2}$ , which is also at the new time level. Conse-

quently, the temporal accuracy of the scheme may be improved by using an iterative technique to obtain better estimates for these otherwise lagged variables.

The continuity equation is discretized in a similar manner with the exception that the expression is centered on the surface elevation positions instead of the  $U$ -velocity positions. The  $x$ -momentum and continuity equations for a line of constant  $\eta$  are grouped together to form a tridiagonal matrix system which is then solved implicitly (represented by the horizontal dashed line in Figure 2). Once the advanced  $U$ -velocity components and surface elevation values have been evaluated for every  $\eta$ -line, the transformed  $y$ -momentum equation is solved explicitly to give the advanced  $V$ -velocities (this is shown diagrammatically in Figure 2 by the horizontal dotted line).

The second half of the ADI cycle is accomplished in a complementary fashion to the first:  $\eta$ -derivatives are expressed at the new time level  $t=(n+1)\Delta t$  whilst gradients with respect to  $\xi$  and non-derivative expressions are held at  $t=(n+\frac{1}{2})\Delta t$ . The  $y$ -momentum and continuity equations are grouped together along each  $\xi$ -line to form tridiagonal matrix systems which are solved implicitly, whereas the  $x$ -momentum expression is solved using a straightforward explicit discretization.

### 5.3. Boundary conditions

In conventional Cartesian schemes the staggered grid structure requires special treatment along the perimeters of the flow domain since velocity components and surface elevations need to be defined *outside* the boundary walls.<sup>3,6,1</sup> In the present investigation a novel boundary approach has been adopted. Here the boundary curve passes through the surface elevation positions and perimeter values of  $\zeta$  are calculated from an explicit discretization of the continuity equation at the start of every half-time step. This technique has several advantages.

- (a) The usual procedure of setting the normal derivative of surface elevation to zero at the boundaries is avoided and therefore the gradient of  $\zeta$  automatically adjusts itself at the wall to suit the hydraulics of the situation. Consequently, wind stress effects can be modelled more accurately.
- (b) The effective stresses are correctly evaluated along the perimeter of the flow field via second-order forward/backward finite difference expressions.
- (c) The values of surface elevation along the boundary obey the continuity equation during transient flow phenomena.

Since the accurate simulation of momentum transfer in recirculating flows requires the use of no-slip constraints at the lateral boundaries,<sup>24</sup> it was decided that the present computational scheme should employ no-slip conditions along all solid walls. Thus the velocity boundary conditions are

$$U_{i_w,j} = -U_{i_w-1,j}, \quad V_{i_w,j} = 0, \quad U_{i,j_w} = 0, \quad V_{i,j_w} = -V_{i,j_w-1}, \quad (21)$$

where the subscripts  $i_w$  and  $j_w$  refer to grid points at the wall and  $i_w - 1$  and  $j_w - 1$  are adjacent points within the flow domain.

Wall surface elevations are calculated from the transformed continuity equation using the fact that  $U_\eta = V_\eta = 0$  along a  $\xi = \text{constant}$  boundary and  $U_\xi = V_\xi = 0$  along an  $\eta = \text{constant}$  boundary. Referring to a 'right-hand'  $\xi = \text{constant}$  boundary, for instance, the explicit finite difference expression which results is

$$\zeta_{i_w,j}^{n+1/2} = \zeta_{i_w,j}^n - \frac{\frac{1}{2}\Delta t D_{i_w,j}}{JAC_{I,J}} (y_{\eta_{t,j}} UXI^n - x_{\eta_{t,j}} VXI^n), \quad (22)$$

where  $I = 2i_w - 1$ ,  $J = 2j - 1$  and

$$\begin{aligned} \text{UXI}^n &= U_{i_w, j}^n - U_{i_w - 1, j}^n && \text{(central difference approximation),} \\ \text{VXI}^n &= \frac{3}{2} V_0^n - 2V_1^n + \frac{1}{2} V_2^n && \text{(backward difference approximation),} \\ V_0^n &= \frac{V_{i_w, j}^n + V_{i_w, j-1}^n}{2} \\ V_1^n &= \frac{V_{i_w - 1, j}^n + V_{i_w - 1, j-1}^n}{2} \\ V_2^n &= \frac{V_{i_w - 2, j}^n + V_{i_w - 2, j-1}^n}{2} \end{aligned} \left. \vphantom{\begin{aligned} \text{UXI}^n \\ \text{VXI}^n \\ V_0^n \\ V_1^n \\ V_2^n \end{aligned}} \right\} \begin{array}{l} \text{(two-point averages are used to} \\ \text{centre the } V\text{-velocities at the} \\ \text{surface elevation/depth nodes).} \end{array}$$

The only modification required for a 'left-hand'  $\zeta = \text{constant}$  boundary is the use of a forward difference quadratic approximation for VXI. Similar finite difference formulae are employed for determining the advanced surface elevations along  $\eta = \text{constant}$  walls.

#### 5.4. Digital filtering

The occurrence of instabilities in boundary-fitted shallow water equation simulations appears to be a common fault of the method. For example, Johnson<sup>8</sup> had to use large values of eddy viscosity coefficient in order to prevent an unbounded growth of grid scale oscillations swamping the numerical solution. Häuser *et al.*,<sup>12</sup> in a numerical study of the *linearized* shallow water equations for a boundary-fitted mesh representative of a tidal harbour, found that their computational scheme became unstable after approximately 15 000 time steps (equivalent to about 24 h of simulation). In this latter case the destabilizing influences could not be attributed to the advective acceleration terms since they were not included in the discretization. Häuser *et al.* were unable to offer an explanation for the instabilities and merely stated that they could not be eliminated by spatial filtering techniques.

In this investigation stability problems were encountered in the form of a gradual growth in surface elevation oscillations for low values of eddy viscosity coefficient; these grid scale variations in surface elevation were eventually transmitted to oscillations in the velocity field. At first this instability was attributed to the imperfect time centring of the advective acceleration terms. However, the problem could not be eliminated by the use of an iteration technique to calculate the advanced non-implicit variables and therefore it was concluded that the instabilities were caused by the boundary conditions.

Since Häuser *et al.*<sup>12</sup> had little success with spatial filtering procedures, a second-order recursive *temporal* filter was employed to eliminate the high-frequency surface elevation noise. The scheme adopted by Butler<sup>25</sup> to control non-linear instabilities in a Cartesian shallow water equation simulation was found to be particularly effective for the present investigation; this involves applying a *lowpass* smoothing filter to damp the high-frequency oscillations at the end of every half-time step. In the present scheme the temporal filter is applied to all primary hydrodynamic variables, i.e.  $\zeta$ ,  $U$  and  $V$ . With reference to the surface elevation  $\zeta$ , the recursive digital filter can be expressed as

$$\zeta^{n+1/2} = a\zeta_1^{n+1/2} + b\zeta^n + c\zeta^{n-1/2}, \quad (23)$$

where  $\zeta_1^{n+1/2}$  represents the latest water level calculated by the ADI algorithm,  $\zeta^{n+1/2}$  is the filtered surface elevation value which is used in subsequent flow calculations and  $a$ ,  $b$  and  $c$  are coefficients which are chosen to damp the high-frequency oscillations such that

$$a + b + c = 1. \quad (24)$$

In order to allow the longer-period wave motions to remain almost undisturbed, the coefficient  $a$  should be as close to unity as possible. Numerical experimentation can be used to select the values of the coefficients in the recursive filter. After studying a wide range of parameters, ranging from  $(a, b, c) = (0.89, 0.1, 0.01)$  to  $(0.4, 0.4, 0.2)$ , Butler<sup>25</sup> chose the coefficients to be  $a = 0.6$ ,  $b = 0.3$  and  $c = 0.1$ ; the same parameters are also used herein.

The filter shown in equation (23) undoubtedly introduces false diffusion into the numerical scheme during transient flow phenomena. If the hydrodynamic solution tends to steady state, however, the effects of the recursive filter become unimportant since the hydrodynamic variables will change even more slowly with time as the equilibrium condition is approached.

## 6. RESULTS

Accurate comparative data from independent studies are necessary in order to validate the computer model. Although field data from river and estuary flows have been widely reported in the literature, very accurate measurements are expensive and difficult to achieve, bearing in mind the organizational problems involving labour and equipment. For the purposes of the studies presented here, data from analytical, alternative numerical and small-scale experimental investigations were compared with predictions from the computational model. The results are presented in three subsections, the first dealing with steady uniform flow in an open rectangular channel, the second considering jet-forced flow in a circular reservoir and the third examining flow in an arbitrarily shaped watercourse. The first two subsections involve comparisons with analytical and alternative numerical models and hence provide benchmark tests for the model. The final subsection demonstrates the versatility of the boundary-fitted technique by examining the flow in an irregularly shaped domain.

### 6.1. Validation against steady uniform flow in a rectangular channel

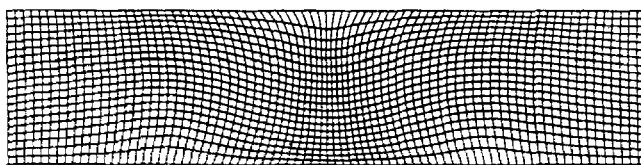
Following Wjibenga,<sup>14</sup> the numerical model was used to simulate steady uniform flow in a parallel-sided channel using a *deliberately* distorted numerically generated co-ordinate mesh. The channel was assumed to be 1000 m long by 240 m wide, with a constant water depth of 5.0 m. The bed slope was specified at 1 in 1000, the Chezy roughness coefficient was taken as 41.42 m<sup>1/2</sup> s<sup>-1</sup> (following Wjibenga) and the eddy viscosity coefficient was set to zero. In contrast to all other simulations presented here, *slip* boundary conditions were applied to the side walls of the flow domain. Besides altering the velocity boundary conditions, the specification of slip walls along the sides of the channel required the finite difference discretization of the continuity boundary condition to be modified. Assuming that the channel walls are formed from  $\eta = \text{constant}$  lines and provided that the co-ordinate system is generated with the slip boundaries parallel to the  $x$ -axis, then the following conditions may be invoked along the side walls of the flow field:

$$V = 0, \quad \frac{\partial V}{\partial \xi} = 0, \quad \frac{\partial y}{\partial \xi} = 0. \quad (25)$$

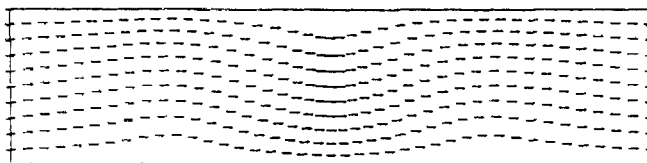
Substituting the above expressions into the transformed continuity equation (12) leads to the surface elevation boundary condition (for the  $\eta = \text{constant}$  walls) being recast as

$$\frac{\partial \zeta}{\partial t} + \frac{1}{J} \left[ y_{\eta} \left( U \frac{\partial D}{\partial \xi} + D \frac{\partial U}{\partial \xi} \right) + x_{\zeta} D \frac{\partial V}{\partial \eta} \right] = 0. \quad (26)$$

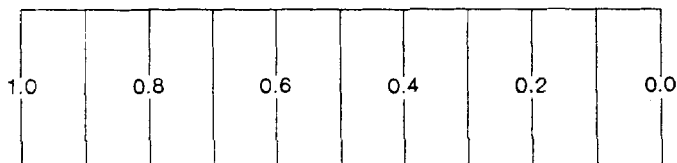
Inflow and outflow velocity conditions were stipulated as  $\partial U / \partial x = 0$  and  $\partial V / \partial x = 0$ .



(a) Physical mesh A



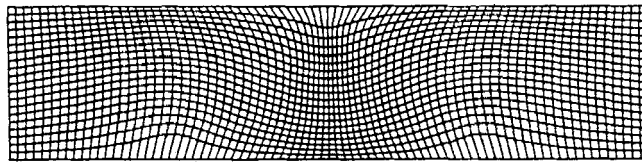
(b) Velocity vectors at steady-state

(c) Surface elevation contours at steady-state  
(metres above downstream boundary)Figure 3. Uniform flow in a rectangular channel (after Wijbenga<sup>14</sup>)

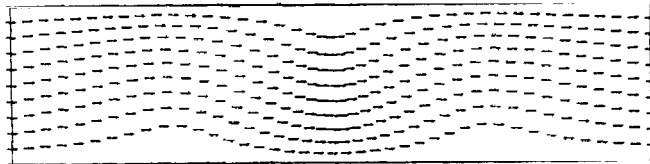
Figures 3(a) and 4(a) illustrate the  $81 \times 21$  node ( $40 \times 10$  flow cell) co-ordinate meshes used in the validation exercise. The co-ordinate systems are representative of those utilized by Wijbenga<sup>14</sup> but are generated so that the grid lines are non-orthogonal. The flow simulations were started from an initial condition  $U = V = 0$ , but in order to reduce the computation time, the initial surface elevation profile was specified as having the same slope as the bed so as to avoid large transient free surface oscillations. Using a time step of 5 s, the numerical scheme converged to equilibrium after approximately 5000 s of simulation time. The velocity vectors in Figures 3(b) and 4(b) show that the flow field is uniform throughout the channel, even though, at first inspection, there is an optical illusion of curved flow due to the location of the velocity vectors at the curvilinear grid points. In fact, the flow features may be better represented by plotting interpolated contours of surface elevation as indicated in Figures 3(c) and 4(c). Here the contours are equispaced parallel lines, indicating a linear drop in surface elevation along the channel (with the same slope as that of the bed), which is expected for uniform flow conditions. Furthermore, the predicted velocities show excellent agreement with the Chezy friction law for normal channel flow,

$$U = C(DS_0)^{1/2} = 41.42 \times (5 \times 10^{-3})^{1/2} = 2.9288 \text{ m s}^{-1}, \quad (27)$$

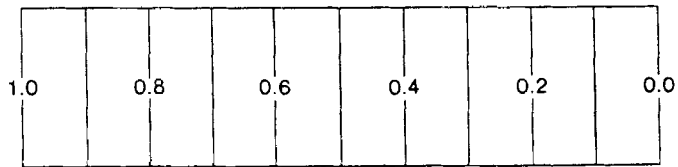
where  $C$  is the Chezy coefficient,  $D$  is the flow depth and  $S_0$  is the bed slope.



(a) Physical mesh B

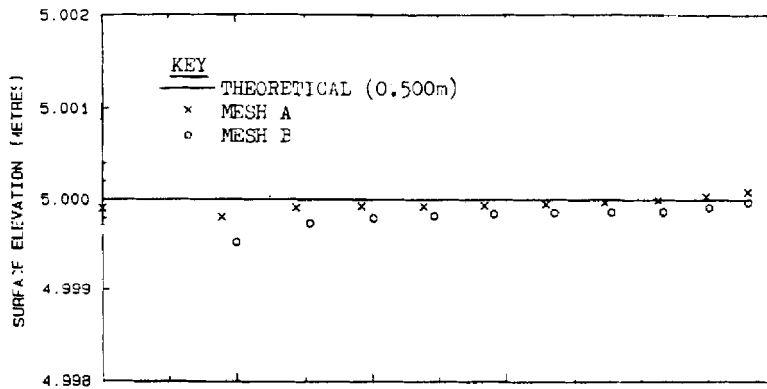


(b) Velocity vectors at steady-state



(c) Surface elevation contours at steady-state (metres above downstream boundary)

Figure 4. Uniform flow in a rectangular channel for a more distorted non-orthogonal mesh



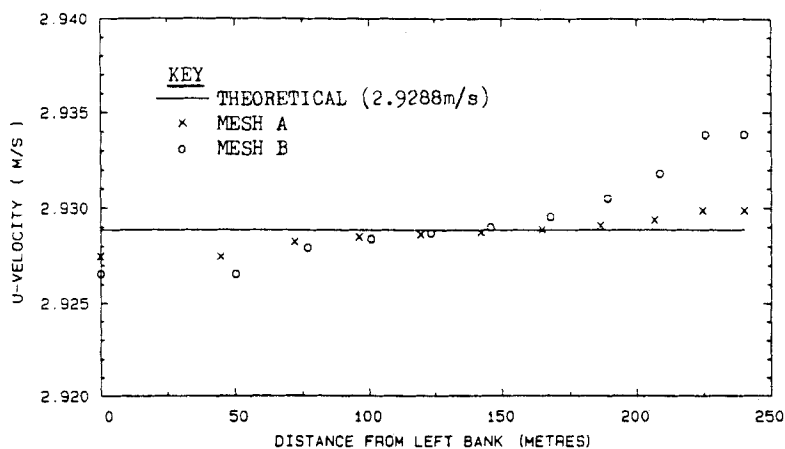


Figure 6. Transverse  $U$ -velocity profile at section halfway along channel

In order to demonstrate the truncation errors in the numerical scheme, Figures 5 and 6 present the transverse surface elevation and  $U$ -velocity profiles at a section halfway along the channel (i.e. 500 m from the upstream inflow boundary). The diagrams indicate that the discretization errors become larger as the co-ordinate mesh becomes more distorted. However, even for the more distorted of the two meshes, the maximum error in surface elevation at the halfway section is less than 0.05 mm whilst the maximum error in the  $U$ -velocity component is less than  $0.005 \text{ m s}^{-1}$ . These errors are considerably smaller than those presented by Wijnbenga<sup>14</sup> for his orthogonal curvilinear shallow water equation solver. This is probably due to the grid arrangement in which the geometrical derivatives ( $x_\xi$ ,  $x_\eta$ ,  $y_\xi$  and  $y_\eta$ ) are evaluated at every flow variable position whereas Wijnbenga's scheme requires some of the geometrical derivatives to be found from two-point interpolation. The main drawback with the present double-mesh system is that the numerical mapping data require four times the storage capacity of Wijnbenga's algorithms.

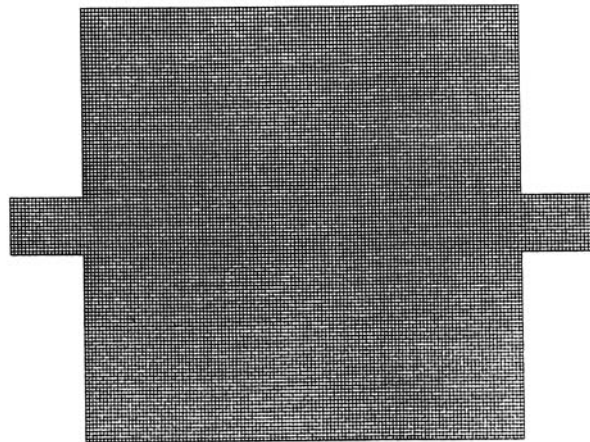
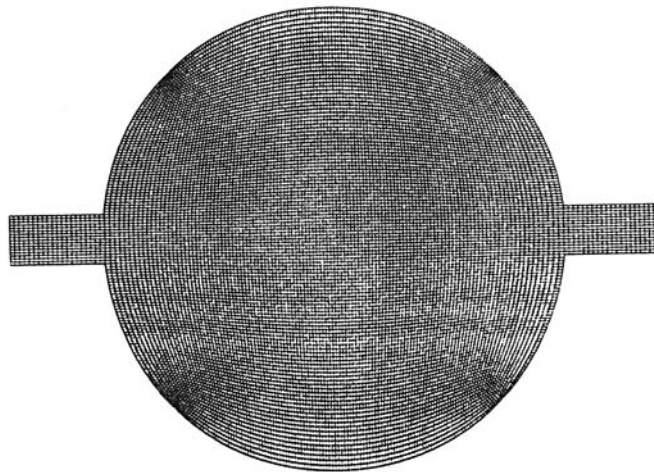
Finally, it should be noted that the small numerical errors depicted in Figures 5 and 6 imply that it is satisfactory to generate boundary-fitted meshes which have quite large cell size variations between adjacent nodes.

### 6.2. Validation against jet-forced flow in a circular reservoir

The prediction of jet-forced flow in a vertical-walled flat-bottomed circular reservoir provides an excellent opportunity to test the discretization of the non-linear terms of the transformed shallow water equations. In this case two-dimensional analytical solutions are available for jet-forced flow in a circle as well as results from alternative numerical studies and experimental data. Three separate circular reservoir geometries were investigated: Dennis's circular container with inlet and outlet placed opposite each other in a symmetric fashion,<sup>26</sup> Mills' geometry with asymmetric alignment of inlet and outlet<sup>27</sup> and the laboratory investigation/Cartesian grid numerical model studied by Falconer.<sup>1,2</sup> For brevity, results are only presented for the first of these geometries; a more detailed intercomparison of jet-forced flow patterns in circular reservoirs is presented by Barber.<sup>23</sup>

Figure 7 illustrates the  $121 \times 121$  node ( $60 \times 60$  flow cell) boundary-fitted co-ordinate system utilized in the present study. The parallel-sided inlet and outlet channels were placed diametrically opposite each other and were designed so that the openings into the circular reservoir



(a) Transformed  $(\xi, \eta)$  plane(b) Physical  $(x, y)$  planeFigure 7. Boundary-fitted co-ordinate system representative of Dennis's symmetrical geometry<sup>26</sup>

subtended an angle of  $\pi/15$  rad (as measured from the centre of the circle). This is representative of the geometry used by Dennis<sup>26</sup> for the numerical investigation of low-Reynolds-number jet-forced flow inside a circle. Dennis did not include inlet or outlet channels and so did not allow for boundary layer effects at the entrance or exit. The circular basin was assumed to have a diameter of 1.5 m, a depth of 0.1 m and an inflow velocity of  $0.1 \text{ m s}^{-1}$ . No-slip boundary conditions were applied to the perimeter walls of the flow domain and the bed friction coefficient  $c_f$ , was set to 0.003. The hydrodynamic simulation employed a time step of 0.025 s, corresponding to a Courant number of approximately 2.5. A constant eddy viscosity of  $7.84 \times 10^{-4} \text{ m}^2 \text{ s}^{-1}$  was utilized across the entire domain, leading to an inlet Reynolds number  $Re_I$ , based upon the eddy viscosity

coefficient of 10.0. The inlet Reynolds number is defined in an identical manner to Mills,<sup>27</sup> i.e.

$$Re_1 = \frac{U_1 \varepsilon R_0}{\tilde{\nu}_t}, \quad (28)$$

where  $U_1$  is the mean inlet velocity,  $\varepsilon$  is half the angle subtended by the inlet,  $R_0$  is the radius of the reservoir and  $\tilde{\nu}_t$  is the horizontal eddy viscosity coefficient. Steady state was attained after approximately 20 000 time steps.

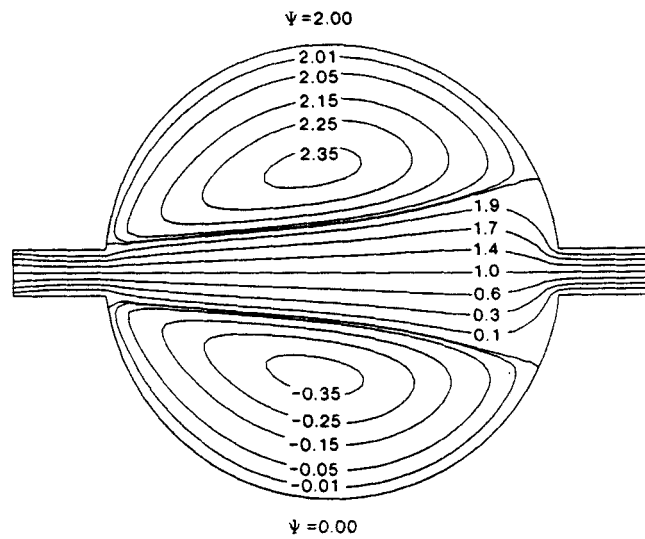
Instead of depicting the circulation using the velocity vector distribution, the flow pattern within the reservoir is better represented by contouring values of numerically integrated depth-averaged streamfunction. The main advantage of this approach is the elimination of an optical illusion of flow following the grid lines which is caused by plotting the velocity vectors at the nodes of the curvilinear co-ordinate grid. Figure 8(a) illustrates the scaled streamfunction contours at steady state determined from the present boundary-fitted primitive variable ( $U, V, \zeta$ ) scheme, whilst Figure 8(b) presents the corresponding circulation patterns calculated using a finite difference solution of the streamfunction/vorticity-transport ( $\psi, \omega$ ) equations in polar form on an algebraically stretched orthogonal mesh.<sup>28, 29</sup> Apart from slight discrepancies near the centre of each gyre, the contours depicted in Figure 8(a) are almost identical to those obtained from the ( $\psi, \omega$ ) simulation. Comparison of the circulation patterns reveals that there is also close agreement between the throughflow streamfunction contours. Moreover, the positions of re-attachment of the separation streamlines ( $\psi = 0.0$  and  $\psi = 2.0$ ) are very similar. It can therefore be concluded that the quadratic upwind differencing methodology (introduced in the discretization of the curvilinear transformed shallow water equations) causes little additional numerical diffusion compared with the central difference advective scheme used by Borthwick and Barber<sup>28, 29</sup> for solving the vorticity transport equation.

### 6.3. Arbitrary river geometry

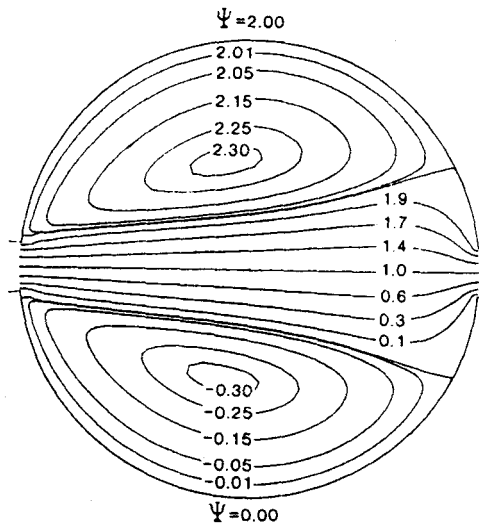
This final subsection demonstrates the versatility of the curvilinear co-ordinate technique by examining the flow in an arbitrarily shaped watercourse with a highly contorted perimeter. In order to demonstrate that the boundary-fitted shallow water equation solver is capable of predicting *large-scale* jet-forced flow phenomena typically encountered in real life studies, the physical mesh shown in Figure 9 represents a 1.5 km long section of river. The mesh consists of  $121 \times 31$  nodes ( $60 \times 15$  flow cells). Numerical experimentation demonstrated that it was beneficial to generate the boundary-fitted system using the control functions  $P$  and  $Q$ . Without the use of these weighting functions the elliptic grid generation equations tended to produce excessively large grid cells in regions of strong concave boundary curvature and very small cells in the vicinity of strong convex boundary curvature.

The irregular bathymetry employed in the study is illustrated in Figure 10, which shows the bed contours in metres below the horizontal datum. It can be seen that the depths vary from 0.5 m at the no-slip perimeters to a maximum of approximately 3.0 m in the centre of the flow domain. The velocity in the narrow inflow jet was set to  $0.5 \text{ m s}^{-1}$ , the Chezy roughness coefficient was assumed to be  $45 \text{ m}^{1/2} \text{ s}^{-1}$  across the entire flow field and the Coriolis parameter was specified as  $f_c = 1.19 \times 10^{-4}$ , corresponding to a latitude of  $55^\circ \text{ N}$ .

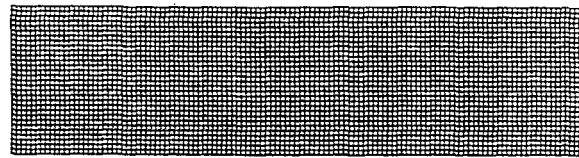
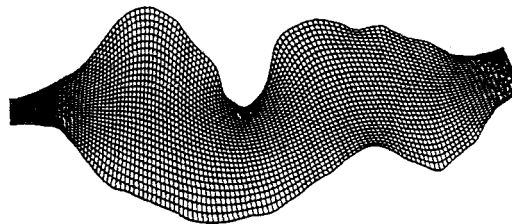
The magnitude of the eddy viscosity coefficient  $\tilde{\nu}_t$ , is critical in determining the resultant circulation patterns. As well as controlling the size and strength of secondary flow phenomena, the eddy viscosity affects the transfer of momentum between the main river channel and the shallower flow areas near the banks and therefore influences the transverse velocity profile across the river. In a numerical study of the flow patterns in a fast-flowing river with a wide flood plain,



(a) Boundary-fitted (U,V,f) approach

(b)  $(\psi, \omega)$  discretisationFigure 8. Streamfunction contours at steady state ( $Re_1 = 10.0$ )

Vreugdenhil and Wjibenga<sup>30</sup> considered eddy viscosities in the range from 5.0 to 1.0  $\text{m}^2 \text{s}^{-1}$  and calibrated their model by comparing the computed longitudinal surface elevation profile against experimental field data. In the present simulation the flow velocities are an order of magnitude smaller than those considered by Vreugdenhil and Wjibenga and therefore the eddy viscosity is

(a) Transformed  $(\xi, \eta)$  plane

Length scale: ——— 200m

(b) Physical  $(x, y)$  plane

Figure 9. Boundary-fitted system for arbitrary river geometry

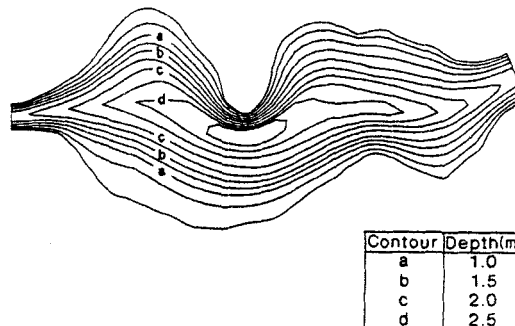
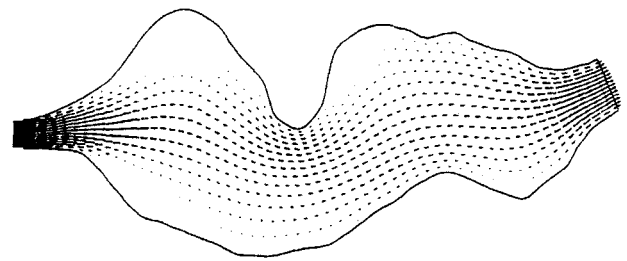




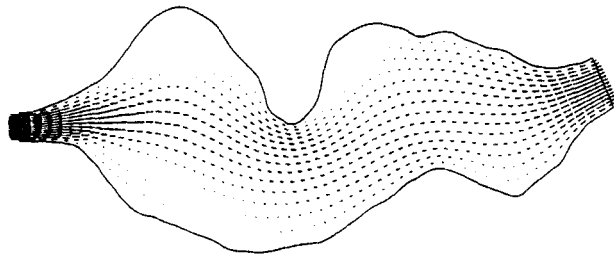
Figure 10. Bed topography for arbitrary river geometry (metres below horizontal datum)



expected to range between  $0.5$  and  $0.1 \text{ m}^2 \text{ s}^{-1}$ . Three separate flow simulations were performed, with constant eddy viscosity coefficients of  $1.0$ ,  $0.5$  and  $0.25 \text{ m}^2 \text{ s}^{-1}$ .

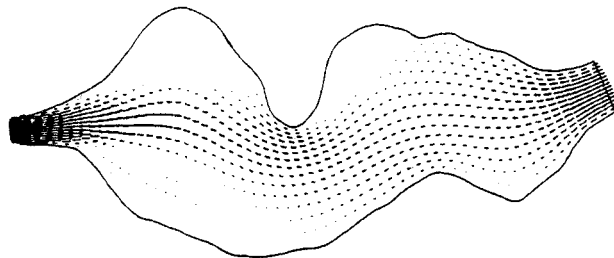
Figure 11 illustrates the predicted steady state velocity distributions across the entire flow domain, while Figure 12 details the circulation patterns in the vicinity of the inflow jet. It is evident that the magnitude of the eddy viscosity coefficient has a dramatic effect upon the level of recirculation in the river. For example, at an eddy viscosity of  $1.0 \text{ m}^2 \text{ s}^{-1}$  Figure 12(a) indicates that the lower recirculation zone is very weak and only extends about  $200 \text{ m}$  downstream of the separation point. However, with an eddy viscosity of  $0.25 \text{ m}^2 \text{ s}^{-1}$  (Figure 12(c)) the lower gyre is more prominent and stretches approximately  $500 \text{ m}$  from the separation point. The increased size of the recirculating eddies is closely related to the reduced divergence of the fast inflow jet.



Length scale:  200m  
 Velocity scale:  1.0ms<sup>-1</sup> (a)  $\tilde{\nu}_t = 1.0 \text{ m}^2/\text{s}$



Length scale:  200m  
 Velocity scale:  1.0ms<sup>-1</sup> (b)  $\tilde{\nu}_t = 0.5 \text{ m}^2/\text{s}$





Length scale:  200m  
 Velocity scale:  1.0ms<sup>-1</sup> (c)  $\tilde{\nu}_t = 0.25 \text{ m}^2/\text{s}$

Figure 11. Velocity vectors at steady state

A further flow simulation using an eddy viscosity of  $0.1 \text{ m}^2 \text{ s}^{-1}$  was attempted, but it was found that the numerical scheme suffered from severe surface elevation instabilities, even when the coefficients of the digital filter had been altered to  $(a, b, c) = (0.2, 0.5, 0.3)$ . It was found that the instabilities were due to excessive cell Reynolds numbers in the inflow jet; consequently, the only method to investigate flows with lower values of eddy viscosity is by increasing the resolution of

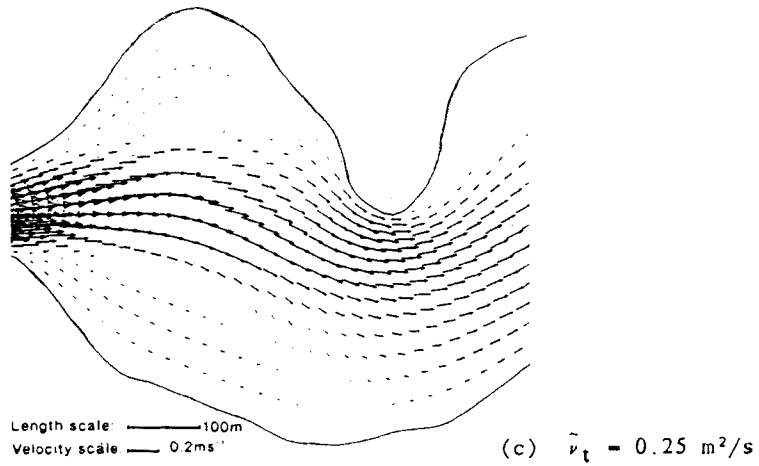
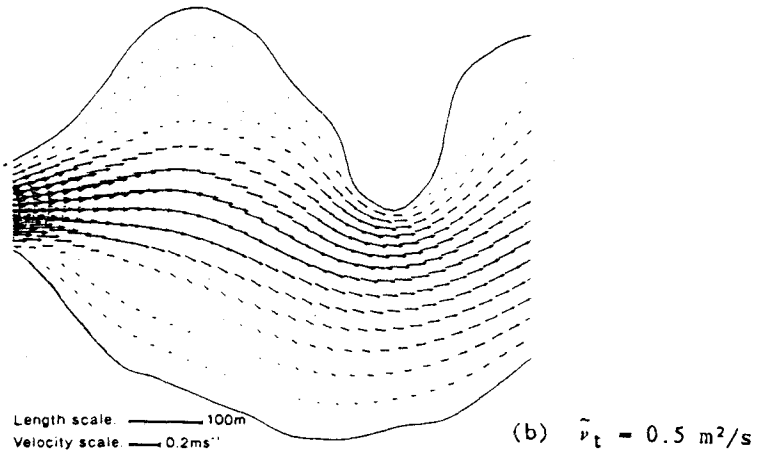
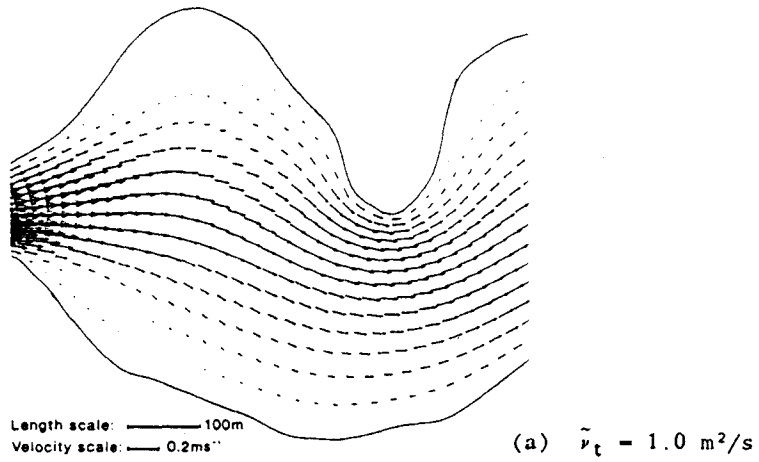


Figure 12. Detail of velocity structure in the inflow jet

the finite difference mesh. In order to demonstrate that the lower limit of the eddy viscosity coefficient is not too severe compared with other numerical schemes, it is worthwhile considering the cell Reynolds number at the centre of the inflow boundary. In this case

$$U = 0.5 \text{ m s}^{-1}, \quad \Delta x \approx 20 \text{ m}$$

and therefore the longitudinal cell Reynolds number for the stable ( $\tilde{\nu}_t = 0.25 \text{ m}^2 \text{ s}^{-1}$ ) simulation is

$$R_c = \frac{U \Delta x}{\tilde{\nu}_t} \approx \frac{0.5 \times 20}{0.25} = 40. \quad (29)$$

Similarly, the unstable ( $\tilde{\nu}_t = 0.1 \text{ m}^2 \text{ s}^{-1}$ ) computation is associated with a cell Reynolds number of approximately 100. The upper limit of  $R_c \approx 40$  in the present scheme compares favourably with other numerical discretizations using curvilinear grids (e.g. Reference 31).

## 7. CONCLUSIONS AND RECOMMENDATIONS

This paper has demonstrated the feasibility of implementing a non-linear shallow water equation solver in conjunction with a non-orthogonal curvilinear co-ordinate system. The present numerical formulation uses Cartesian velocity components as dependent variables and solves the transformed shallow water equations using a semi-implicit alternating direction finite difference scheme. It has been found that a combination of weighted central and second-order upwind difference approximations is required for the cross-advective acceleration terms of the momentum equations in order to achieve a stable discretization. Nevertheless, stability problems are still encountered when low values of eddy viscosity and severe mesh distortion prevail, and it has been found necessary to treat these instabilities with a second-order digital lowpass smoothing filter.

The results indicate that the boundary-fitted shallow water equation approach offers a flexible computational method for predicting the hydrodynamic conditions in awkwardly shaped flow regimes and it is envisaged that the technique could therefore provide water resources engineers with a powerful alternative to patched/nested finite difference methods. Boundary-fitted techniques are ideally suited to studying flow domains with narrow-channelled inlets or outlets since the co-ordinate system can be made to expand smoothly away from the confined area. This is in contrast to patched finite difference schemes which undergo a sharp transition in mesh size between grid domains.

In the future, boundary-fitted co-ordinate systems may offer the intriguing possibility of accurately modelling flows in estuaries where there are large changes in the cross-sectional area of the flow during each tidal cycle. Conventional techniques for dealing with changes in wetted plan-form area using flooding/drying cells can often produce troublesome oscillations in water surface elevation at mesh points near the boundary. Time-dependent boundary-fitted co-ordinate systems in which the grid constantly adapts to the changing shape of the wetted perimeter may overcome this difficulty by removing the need for a flooding/drying technique entirely. However, as yet, no published research has been presented along these lines.

## ACKNOWLEDGEMENT

The second author (R.W.B.) would like to acknowledge support from the U.K. Science and Engineering Research Council.

## APPENDIX: NOMENCLATURE

$a, b, c$	coefficients of digital second-order filter
$C$	Chezy roughness coefficient
$c_f$	bed friction coefficient
$D$	total water depth, $D = h + \zeta$
$f_c$	Coriolis parameter
$f$	scalar variable used in demonstration of spatial derivative transformation procedure
$g$	acceleration due to gravity
$h$	bed elevation below arbitrary horizontal datum
$i, j$	finite difference indices for hydrodynamic variables
$I, J$	finite difference indices for geometric variables
$J$ or $JAC$	Jacobian
$n$	Manning roughness coefficient or time step index
$P, Q$	weighting functions for grid generation equations
$R$	hydraulic radius
$R_c$	cell Reynolds number
$S_0$	bed slope
$t$	time
$T_{xx}, T_{xy}, T_{yy}$	effective stresses
$U, V$	depth-averaged velocity components in $x$ - and $y$ -direction respectively
$x, y$	orthogonal co-ordinates in physical plane

*Greek letters*

$\alpha, \beta, \gamma$	coefficients of transformed grid generation equations
$\Delta t$	time step
$\Delta x$	grid spacing in physical plane
$\zeta$	water surface elevation above arbitrary horizontal datum
$\nu$	fluid kinematic viscosity
$\tilde{\nu}_t$	'depth-averaged' eddy viscosity coefficient
$\xi, \eta$	non-orthogonal curvilinear co-ordinates
$\rho$	fluid density
$\tau_{bx}, \tau_{by}$	bed shear stress components in $x$ - and $y$ -direction respectively
$\tau_{wx}, \tau_{wy}$	wind shear stress components in $x$ - and $y$ -direction respectively
$\psi$	streamfunction
$\omega$	vorticity

## REFERENCES

1. R. A. Falconer, 'Mathematical modelling of jet-forced circulation in reservoirs and harbours', *Ph.D. Thesis*, Imperial College, London, 1976.
2. R. A. Falconer, 'Numerical modelling of tidal circulation in harbours', *J. Waterway, Port, Coastal Ocean Div., Proc. ASCE*, **106**, 31-48 (1980).
3. J. J. Leendertse, 'Aspects of a computational model for long-period water-wave propagation', *RM-5294-PR*, The Rand Corporation, 1967.
4. M. B. Abbott, A. Damsgaard and G. S. Rodenhuis, 'System 21, "Jupiter" (a design system for two-dimensional nearly-horizontal flows)', *J. Hydraul. Res.*, **11**, 1-28 (1973).
5. S. Hodgins, 'An improved computational method for the shallow water wave equations based on the Leendertse (1967) finite-difference scheme', *Rep. STF60A-77058*, River and Harbour Laboratory, Norwegian Institute of Technology, Trondheim, 1977.



6. J. Kuipers and C. B. Vreugdenhil, 'Calculations of two-dimensional horizontal flow', *Res. Rep. S163, Part 1*, Delft Hydraulics Laboratory, 1973.
7. T. J. Weare, 'Finite element or finite difference methods for the two-dimensional shallow water equations?', *Comput. Methods Appl. Mech. Eng.*, **7**, 351–357 (1976).
8. B. H. Johnson, 'VAHM—a vertically averaged hydrodynamic model using boundary-fitted coordinates', *Misc. Paper HL-80-3*, U.S. Army Engineer Waterways Experiment Station Hydraulics Laboratory, Vicksburg, MS, 1980.
9. B. H. Johnson, 'Numerical modelling of estuarine hydrodynamics on a boundary-fitted coordinate system', in J. F. Thompson (ed.), *Numerical Grid Generation*, 1982, pp. 409–436.
10. B. H. Johnson, A. B. Stein and J. F. Thompson, 'Modelling of flow and conservative substance transport on a boundary-fitted coordinate system', *Proc. IAHR Symp. on Refined Modelling of Flows, Vol. 2*, Paris, 1982, pp. 509–518.
11. J. Häuser, H. G. Paap, D. Eppel and A. Mueller, 'Solution of shallow water equations for complex flow domains via boundary fitted coordinates', *Int. j. numer. methods fluids*, **5**, 727–744 (1985).
12. J. Häuser, H. G. Paap, D. Eppel and S. Sengupta, 'Boundary conformed coordinate systems for selected two-dimensional fluid flow problems. Part 2: Application of the BFG method', *Int. j. numer. methods fluids*, **6**, 529–539 (1986).
13. R. Raghunath, S. Sengupta and J. Häuser, 'A study of the motion in rotating containers using a boundary-fitted coordinate system', *Int. j. numer. methods fluids*, **7**, 453–464 (1987).
14. J. H. A. Wijnbenga, 'Determination of flow patterns in rivers with curvilinear coordinates', *Proc. 21st IAHR Congr.*, Melbourne, August 1985; reprinted as *Publ. No. 352*, Delft Hydraulics Laboratory, October 1985.
15. J. H. A. Wijnbenga, 'Steady depth-averaged flow calculations on curvilinear grids', *Proc. 2nd Int. Conf. on the Hydraulics of Floods and Flood Control*, Cambridge, September 1985, pp. 373–387.
16. J. B. T. M. Willemsse, G. S. Stelling and G. K. Verboom, 'Solving the shallow water equations with an orthogonal coordinate transformation', *Proc. Int. Symp. on Computational Fluid Dynamics*, Tokyo, September 1985; reprinted as *Commun. No. 356*, Delft Hydraulics Laboratory, January 1986.
17. J. F. Thompson, F. C. Thames and C. W. Mastin, 'Automatic numerical generation of body-fitted curvilinear coordinate system for field containing any number of arbitrary two-dimensional bodies', *J. Comput. Phys.*, **15**, 299–319 (1974).
18. J. F. Thompson, F. C. Thames and C. W. Mastin, 'TOMCAT—a code for numerical generation of boundary-fitted curvilinear coordinate systems on fields containing any number of arbitrary two-dimensional bodies', *J. Comput. Phys.*, **24**, 274–302 (1977).
19. H. Schlichting, *Boundary-layer Theory*, 6th edn, McGraw-Hill, New York, 1968.
20. Y. P. Sheng and J. E. Hirsh, 'Numerical solution of shallow water equations in boundary fitted grids', *Tech. Memo. 84-15*, Aeronautical Research Associates of Princeton, Inc., Princeton, NJ, 1984.
21. G. S. Stelling, 'On the construction of computational methods for shallow water flow problems', *Ph.D. Thesis*, Delft University of Technology, 1983.
22. G. S. Stelling and J. B. T. M. Willemsse, 'Remarks about a computational method for shallow water equations that works in practice', J. G. Verwer (ed.), *Colloquium Topics in Applied Numerical Analysis, CWI Syllabus No. 5*, Centrum voor Wiskunde en Informatica, Amsterdam, 1984, pp. 337–362.
23. R. W. Barber, 'Numerical modelling of jet-forced circulation in reservoirs using boundary-fitted coordinate systems', *Ph.D. Thesis*, University of Salford, 1990.
24. G. H. Lean and T. J. Weare, 'Modelling two-dimensional circulating flow', *J. Hydraul. Div., Proc. ASCE*, **105**, 17–26 (1979).
25. H. L. Butler, 'Numerical simulation of tidal hydrodynamics, Great Egg Harbour and Corson Inlets, New Jersey', *Tech. Rep. H-78-11*, U.S. Army Engineer Waterways Experiment Station Hydraulics Laboratory, Vicksburg, MS, 1978.
26. S. C. R. Dennis, 'Application of the series truncation method to two-dimensional internal flows', *Proc. 4th Int. Conf. on Numerical Methods in Fluid Dynamics*, Springer, New York, 1974, pp. 146–151.
27. R. D. Mills, 'Computing internal viscous flow problems for the circle by integral methods', *J. Fluid. Mech.*, **79**, 609–624 (1977).
28. A. G. L. Borthwick and R. W. Barber, 'Jet-forced flow inside a circle at very low Reynolds numbers', *Rep. No. 88/224*, Department of Civil Engineering, University of Salford, December 1988.
29. A. G. L. Borthwick and R. W. Barber, 'Prediction of low Reynolds number jet-forced flow inside a circle using the Navier–Stokes equations', *Int. J. Eng. Fluid Mech.*, **3**, 323–343 (1990).
30. C. B. Vreugdenhil and J. H. A. Wijnbenga, 'Computation of flow patterns in rivers', *J. Hydraul. Div., Proc. ASCE*, **108**, 1296–1310 (1982).
31. M. J. Officier, C. B. Vreugdenhil and H. G. Wind, 'Applications in hydraulics of numerical solutions of the Navier–Stokes equations', in C. Taylor, J. A. Johnson and W. R. Smith (eds), *Recent Advances in Numerical Methods in Fluids, Vol. 5*, Pineridge, Swansea, 1986, pp. 115–147.